J. Adv. Model. Earth Syst., **Vol. 2,** Art. #7, 13 pp.

Application of the Concepts of Rossby Length and Rossby Depth to Tropical Cyclone Dynamics

Wayne H. Schubert and Brian D. McNoldy

Department of Atmospheric Science, Colorado State University, Fort Collins, Colorado, USA

Manuscript submitted 19 July 2010; in final form 21 September 2010

This paper examines the usefulness of the complementary concepts of Rossby length and Rossby depth. These concepts are discussed in the context of idealized analytical solutions of the transverse circulation equation that arises in the balanced vortex model of tropical cyclones. When its coefficients can be considered as constants, this elliptic partial differential equation for the transverse circulation is solved in three different ways: (i) First perform a vertical transform to obtain a radial structure equation, from which arises the concept of a spectrum of Rossby lengths; (ii) First perform a radial transform to obtain a vertical structure equation, from which arises the concept of a spectrum of Rossby depths; (iii) First solve the elliptic PDE directly, without regard to boundary conditions, and then enforce the boundary conditions using the method of image circulations. For weak vortices, Rossby lengths are large and Rossby depths are small, so that the secondary circulation is horizontally elongated and vertically compressed. For strong vortices, Rossby lengths are small and Rossby depths are large, so that the secondary circulation is more vertically elongated and so horizontally compressed that some of the eyewall updraft can return as subsidence in the eye. For strong vortices, the secondary circulation associated with eyewall diabatic heating can be significantly suppressed by the large inertial stability in the interior of the vortex. The large variations of Rossby depth with vortex strength also have important implications concerning how far Ekman pumping can penetrate vertically; only strong vortices have large enough Rossby depths to allow Ekman pumping to penetrate deep into the troposphere.

DOI:10.3894/JAMES.2010.2.7

1. Introduction

Figure 1 shows an AMSR-E 89 GHz microwave image of the precipitation structure of Typhoon Choi-Wan when it was located approximately 450 km north of Guam and had a nearly-closed concentric eyewall structure. At this time (0353 UTC on 15 September 2009), CloudSat's 94 GHz Cloud Profiling Radar had a fortuitous pass directly over the 65 m s^{-1} storm. The CloudSat ground track is indicated by the thin red line. Figure 2 shows the CloudSat north-south vertical cross-section of radar reflectivity, with north to the right. In the top panel, the horizontal scale is compressed by a factor of 6.7 to exaggerate the vertical structure. The inner eyewall is very narrow and slopes outward between radii of 10 and 25 km, while the outer, nearly concentric secondary eyewall is much wider, as indicated on the north side, for example, by the high radar reflectivity values (red) penetrating above z = 10 km between radii of 80 and 130 km. In the bottom panel, only the region inside a radius of 50 km is shown, but the aspect ratio is one-to-one, clearly revealing the approximate 45° baroclinic tilt of the eyewall updraft and the upper level cloud overhang at the outer edge of the eye.

Vortices such as Typhoon Choi-Wan tend to be balanced in the sense that they are continuously evolving from one gradient balanced state to another, which implies that the transverse circulation is determined by the solution of a second order partial differential equation in the (r, z)-plane. According to this "transverse circulation equation," first derived by Eliassen (1952), the streamfunction for the radial and vertical motion is determined by the radial derivative of the diabatic heating, the vertical derivative of the frictional torque, and the three variable coefficients A, B, C, which are the static stability, the baroclinity, and the inertial stability. Although solutions of the transverse circulation equation generally yield radial and vertical velocities that are much weaker than the azimuthal velocity, the radial and vertical directions are the directions of large gradients, so the relatively weak transverse circulation is crucial for vortex evolution. In his classic 1952 paper, Eliassen presented the principal part of the Green's function solutions of the constant coefficient version of the transverse circulation equation for the case in which $\partial Q/\partial r$ is localized and for the case in which the diabatic heating Q itself is localized in the (r, z)-plane. These Green's function solutions clearly illustrate how the strength and shape of the transverse circulation depend on the coefficients A, B, C.

To whom correspondence should be addressed.
Wayne H. Schubert, Department of Atmospheric Science, Colorado State University, Fort Collins, CO 80523-1371, USA
waynes@atmos.colostate.edu

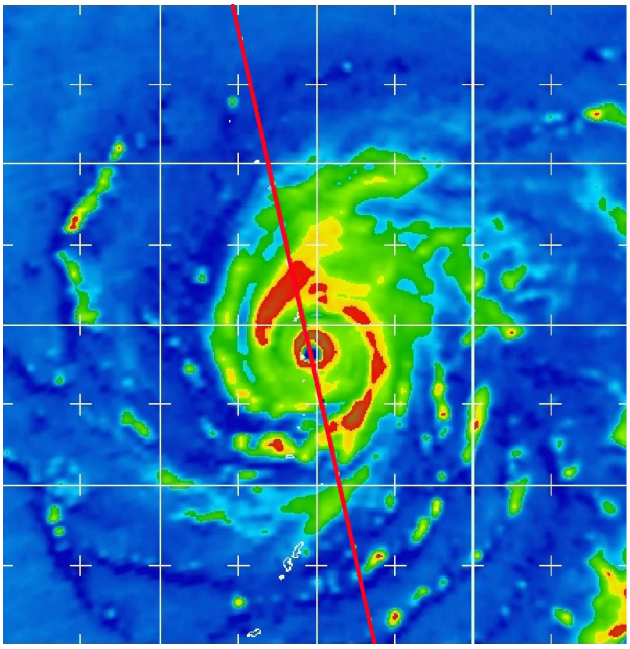

Figure 1. This 89 GHz microwave image from AMSR-E shows the precipitation structure of Typhoon Choi-Wan at the time of the CloudSat overpass shown in Fig. 2. The CloudSat ground track is indicated by the red line. The warmer colors in the plot indicate more intense convection. The spatial resolution of AMSR-E's 89 GHz channel is 5.4 km. The + marks are every 1 degree of longitude and latitude, with the south edge at 14N and the west edge at 142E. Image courtesy of NRL Monterey.

In the present paper we consider idealized vortex structures and idealized vertical structures of Q that allow the transverse circulation equation to be solved analytically via three different methods. These simple theoretical arguments illustrate the usefulness of the complementary concepts of Rossby length (also sometimes referred to as the "Rossby radius of deformation") and Rossby depth, and thereby elaborate on ideas discussed in the extensive literature on applications of the balanced vortex model to tropical cyclones (e.g., Ooyama 1969, Sundqvist 1970a,b, Smith 1981, Shapiro and Willoughby 1982, Schubert and Hack 1982, Hack and Schubert 1986, Nolan et al. 2007, Vigh and Schubert 2009, Pendergrass and Willoughby 2009, and Willoughby 2009).

The paper is organized in the following way. In Section 2, the balanced vortex model and the associated transverse circulation equation are presented. Section 3 discusses the solution of the transverse circulation equation using a method in which the partial differential equation is first transformed in the vertical to obtain a set of ordinary differential equations for the radial structure of the various vertical modes. The concept of a spectrum of Rossby lengths naturally arises from this approach. Section 4 examines the same elliptic problem of Section 3, but using a different mathematical technique. The partial differential equation for the transverse circulation is first transformed in the radial direction, yielding a set of ordinary differential equations for the vertical structure of the various radial modes. The concept of a spectrum of Rossby depths naturally arises from this approach. The methods of Sections 3 and 4 are complementary in the sense that they yield two different mathematical representations (and two complementary physical interpretations) of the same transverse circulation. These two analytical solutions of the transverse circulation equation aid in understanding how the general features of the transverse circulation change as a vortex intensifies and the inertial stability C becomes very large in the inner region of the vortex. The general rule that vortex intensification leads to decreasing Rossby lengths and increasing Rossby depths also aids in understanding the changing influence of the boundary conditions on the overall circulation. Section 5 examines a third approach to the solution of the transverse circulation equation. This third approach, more in the spirit of Green's function methods, has the advantage that baroclinic effects are more easily included. The results obtained with this approach indicate that baroclinic effects play a minor role in determining the strength of the transverse circulation, but play a major role in determining its shape, especially the large outward tilt of the eyewall seen in storms such as Typhoon Choi-Wan. As discussed in Section 6, the concepts of Rossby length and Rossby depth can also aid in understanding the upward penetration of Ekman pumping, which appears to be quite sensitive to vortex strength. This indicates that the role of Ekman pumping in forcing deep convection increases as a vortex intensifies. Some concluding remarks about vortex preconditioning are presented in Section 7.

2. Balanced vortex model

We consider inviscid, axisymmetric, quasi-static, gradient-balanced motions of a stratified, compressible atmosphere on an f-plane. As the vertical coordinate we use $z = (c_p\theta_0/g)[1-(p/p_0)^\kappa]$, where $p_0 = 1000$ hPa and $\theta_0 = 300$ K are constant reference values of pressure and potential temperature. The governing equations for the balanced vortex model are

$$\left(f + \frac{v}{r}\right)v = \frac{\partial\phi}{\partial r}, \tag{2.1}$$

$$\frac{\partial v}{\partial t} + u\left(f + \frac{\partial(rv)}{r\partial r}\right) + w\frac{\partial v}{\partial z} = 0, \tag{2.2}$$

$$\frac{\partial\phi}{\partial z} = \frac{g}{\theta_0}\theta, \tag{2.3}$$

$$\frac{\partial(ru)}{r\partial r} + \frac{\partial(\rho w)}{\rho\partial z} = 0, \tag{2.4}$$

$$\frac{\partial\theta}{\partial t} + u\frac{\partial\theta}{\partial r} + w\frac{\partial\theta}{\partial z} = \frac{Q}{\Pi}, \tag{2.5}$$

where u and v are the radial and azimuthal components of velocity, w is the 'vertical velocity', ϕ is the geopotential, f is the constant Coriolis parameter, $\rho(z) = \rho_0[1-(gz/c_p\theta_0)]^{(1-\kappa)/\kappa}$ is the pseudodensity, $\rho_0 = p_0/(R\theta_0)$ is the constant reference density, $\Pi = c_p(p/p_0)^\kappa$ is the Exner function, and Q is the diabatic heating.

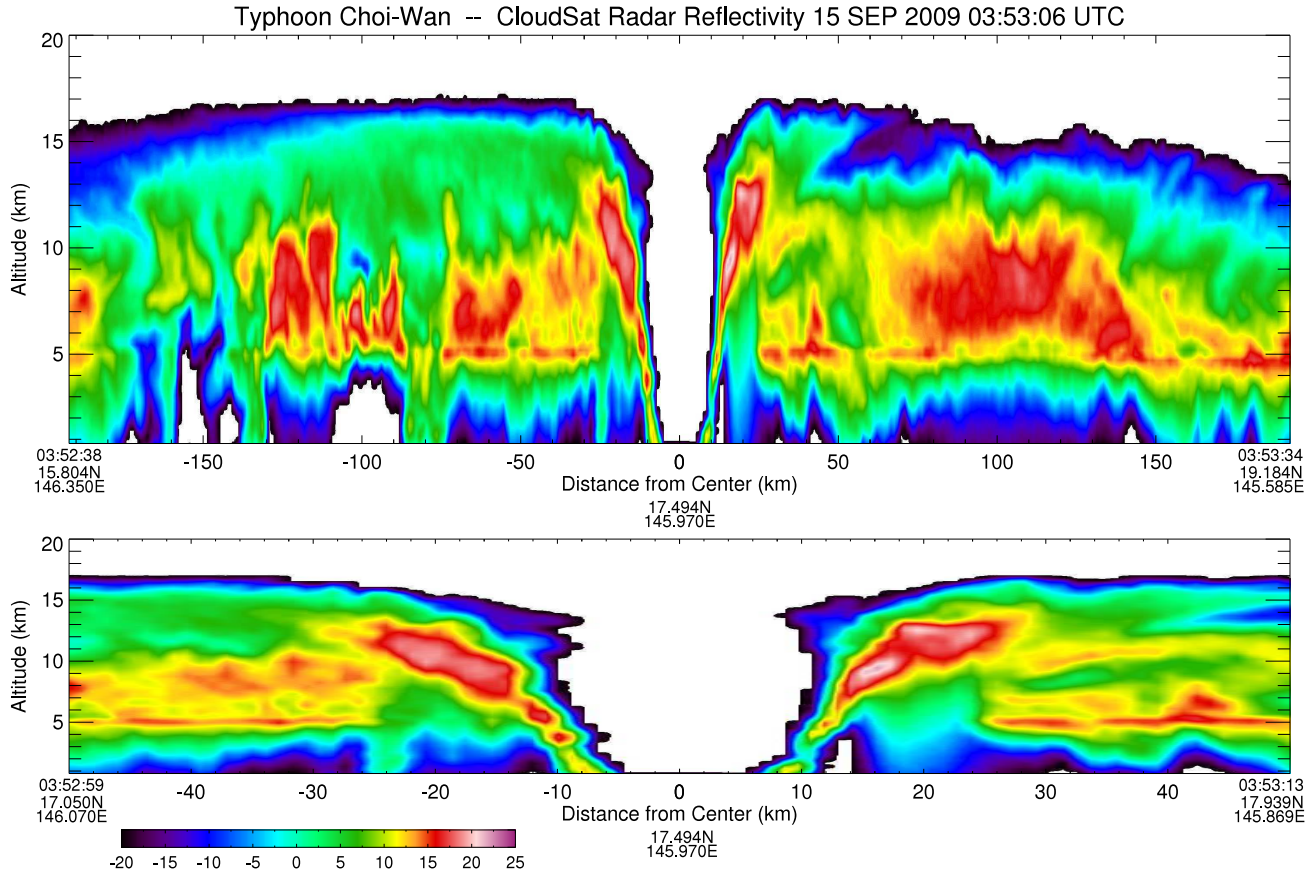

Figure 2. CloudSat's 94 GHz Cloud Profiling Radar pass directly over Typhoon Choi-Wan on 15 September 2009 at 0353 UTC. This figure shows a north-south vertical cross-section of radar reflectivity for the 65 m s^{-1} storm (north is to the right) when it was located approximately 450 km north of Guam. In the top panel, the horizontal scale is compressed by a factor of 6.7 to exaggerate the vertical structure. In the bottom panel, only the region inside a radius of 50 km is shown (which excludes the secondary eyewall), but the aspect ratio is one-to-one, so features are presented as they would appear in nature. Reflectivity values less than −20 dBZ have been removed for clarity. The cross-track horizontal resolution of CloudSat is 1.4 km. Radar data are courtesy of the NASA CloudSat Project.

Multiplying the azimuthal wind equation (2.2) by $(f + 2v/r)$ and the thermodynamic equation (2.5) by (g/θ_0), and then making use of the gradient wind equation (2.1) and the hydrostatic equation (2.3), we obtain

$$\frac{\partial \phi_t}{\partial r} - B\rho w + C\rho u = 0, \tag{2.6}$$

$$\frac{\partial \phi_t}{\partial z} + A\rho w - B\rho u = \frac{g}{\theta_0}\dot{\theta}, \tag{2.7}$$

where $\phi_t = \partial\phi/\partial t$ is the geopotential tendency, $\dot{\theta} = Q/\Pi$, and where the static stability A, the baroclinity B, and the inertial stability C are given by

$$\begin{aligned} \rho A &= \frac{g}{\theta_0}\frac{\partial \theta}{\partial z}, \\ \rho B &= -\frac{g}{\theta_0}\frac{\partial \theta}{\partial r} = -\left(f + \frac{2v}{r}\right)\frac{\partial v}{\partial z} = -\frac{\partial m^2}{r^3 \partial z}, \\ \rho C &= \left(f + \frac{2v}{r}\right)\left(f + \frac{\partial (rv)}{r\partial r}\right) = \frac{\partial m^2}{r^3 \partial r}. \end{aligned} \tag{2.8}$$

Note that B can be expressed in terms of θ or v because of thermal wind balance, and that B and C can also be concisely expressed in terms of the absolute angular momentum $m = rv + \frac{1}{2}fr^2$. We can now regard (2.4), (2.6), and (2.7) as a system in ϕ_t, u, w. One way of proceeding from this system is to make use of (2.4) to express the transverse circulation (u, w) in terms of the streamfunction ψ by

$$\rho u = -\frac{\partial \psi}{\partial z} \quad \text{and} \quad \rho w = \frac{\partial (r\psi)}{r\partial r}. \tag{2.9}$$

Note that we have rather loosely used the term 'streamfunction' for ψ. More precisely, the streamfunction for the transverse mass flux is $r\psi$, not ψ. We have chosen not to absorb the r factor into the definition of ψ because keeping the r factor separate is mathematically convenient in deriving the modified Bessel equation (3.6) and in using the Hankel transform pair (4.1) and (4.2). We now eliminate ϕ_t by taking $(\partial/\partial r)(2.7) - (\partial/\partial z)(2.6)$ to obtain the transverse circulation equation given in the top two lines of (2.10). Assuming that w vanishes at the bottom $(z = 0)$ and top $(z = z_T)$ boundaries, that u vanishes at $r = 0$, and that $ru \to 0$ as $r \to \infty$, the

resulting elliptic problem for the transverse circulation can be concisely stated as

$$\frac{\partial}{\partial r}\left(A\frac{\partial(r\psi)}{r\partial r}+B\frac{\partial\psi}{\partial z}\right) + \frac{\partial}{\partial z}\left(B\frac{\partial(r\psi)}{r\partial r}+C\frac{\partial\psi}{\partial z}\right)=\frac{g}{\theta_0}\frac{\partial\dot{\theta}}{\partial r}, \tag{2.10}$$

$$\psi(0,z)=0,\quad \psi(r,0)=0,\quad \psi(r,z_T)=0,$$

$$r\psi(r,z)\to 0 \quad \text{as} \quad r\to\infty.$$

After solving (2.10) for ψ, we can compute u and w from (2.9), and then predict a new v-field from (2.2) or a new θ-field from (2.5), the two predictions being consistent with the thermal wind equation given in the middle entry of (2.8). Note that the problem (2.10) is derived from inviscid dynamics. In Section 6 we shall modify the lower boundary condition in (2.10) in order to examine the upward penetration of Ekman pumping.

From (2.8) it can easily be shown that

$$-\frac{B}{A}=\frac{\partial\theta/\partial r}{\partial\theta/\partial z}=\left(\frac{dz}{dr}\right)_\theta, \tag{2.11}$$

which is the slope of the z-surface with respect to the θ-surface, and that

$$-\frac{B}{C}=\frac{\partial m/\partial z}{\partial m/\partial r}=\left(\frac{dr}{dz}\right)_m, \tag{2.12}$$

which is the slope of the r-surface with respect to the absolute angular momemtum surface ($m=rv+\frac{1}{2}fr^2$). When $B=0$, the θ-surfaces are parallel to the z-surfaces and the m-surfaces are parallel to the r-surfaces (i.e., vertical). As we shall see, the ratio A/C determines, in large part, the effective Rossby length and the effective Rossby depth, both of which can vary over a wide range in tropical cyclones.

In Sections 3 and 4 we consider the response to a $\dot{\theta}(r,z)$ distribution that corresponds to an annular volume of eyewall diabatic heating, i.e., $\dot{\theta}(r,z)$ is assumed to vanish everywhere except in the radial range $r_1<r<r_2$, where r_1 and r_2 are constants. Within this annular volume the diabatic heating is assumed to be independent of r and to have the vertical dependence $\dot{\Theta}(z)$. Thus, $\dot{\theta}(r,z)$ is piecewise constant in the radial direction, with the mathematical form

$$\dot{\theta}(r,z)=\begin{cases}\dot{\Theta}(z) & r_1<r<r_2,\\ 0 & \text{otherwise.}\end{cases} \tag{2.13}$$

With these assumptions, the right hand side of (2.10) vanishes everywhere except along the inside and outside edges of the eyewall, where $|\partial\dot{\theta}(r,z)/\partial r|$ becomes infinitely large over an infinitesimally thin layer. Thus, the total secondary circulation will consist of a chain of counterclockwise turning gyres on the inside edge of the eyewall and a chain of clockwise turning gyres on the outside edge of the eyewall. For the vertical dependence of the diabatic heating we choose

$$\dot{\Theta}(z)=\dot{\Theta}_{\max}\begin{cases}\sin\left(\frac{\pi(z-z_1)}{z_2-z_1}\right) & z_1\le z\le z_2,\\ 0 & \text{otherwise,}\end{cases} \tag{2.14}$$

where z_1, z_2, and $\dot{\Theta}_{\max}$ are constants.

3. Arriving at ψ via the concept of Rossby length

The problem (2.10) is too complicated to solve analytically in the general case when the coefficients A, B, and C vary with r and z in complicated ways. However, we can begin to gain physical insight into the solution of (2.10) by considering the case where $B=0$ (the case $B\neq 0$ is deferred until Section 5), and A and C are constant. This assumption of constant coefficients is useful for gaining physical understanding through analytic solutions; it is more justifiable for the static stability A than the inertial stability C, which tends to be greatly enhanced in the core of intense hurricanes.

In the case of constant coefficients, there are several techniques that can be used to solve (2.10): (i) A vertical sine transform followed by solution of a radial structure equation; (ii) A radial Hankel transform followed by solution of a vertical structure equation; (iii) The method of direct solution, ignoring boundary conditions, followed by the method of images to satisfy boundary conditions. Method (i), which is discussed in this section, leads naturally to physical interpretations based on Rossby length. In contrast, method (ii), which is discussed in Section 4, leads naturally to physical interpretations based on Rossby depth. Method (iii), which is discussed in Section 5, has the advantage of yielding physical understanding through both the Rossby length and Rossby depth, if one restricts the discussion to simple solutions that are valid away from the axis of symmetry. Since these simple solutions do not satisfy the boundary conditions, the method of images needs to be introduced to understand the role of boundary conditions, which can often be an important part of the complete transverse circulation problem.

When A and C are constant and $B=0$, (2.10) reduces to

$$A\frac{\partial}{\partial r}\left(\frac{\partial(r\psi)}{r\partial r}\right)+C\frac{\partial^2\psi}{\partial z^2}=\frac{g}{\theta_0}\frac{\partial\dot{\theta}}{\partial r}. \tag{3.1}$$

Noting the top and bottom boundary conditions for $\psi(r,z)$, we seek solutions of (3.1) via the Fourier sine transform pair, i.e.,

$$\psi(r,z)=\sum_{n=1}^{\infty}\psi_n(r)\sin\left(\frac{n\pi z}{z_T}\right), \tag{3.2}$$

$$\psi_n(r)=\frac{2}{z_T}\int_0^{z_T}\psi(r,z)\sin\left(\frac{n\pi z}{z_T}\right)dz, \tag{3.3}$$

where the Fourier coefficients $\psi_n(r)$ give the radial structure of each vertical mode n. A similar transform pair exists for $\dot{\theta}(r,z)$ and its Fourier coefficients $\dot{\theta}_n(r)$. To take the Fourier

sine transform of (3.1), we first multiply it by $\sin(n\pi z/z_T)$ and integrate over z from 0 to z_T. The integral originating from the second term in (3.1) is then integrated by parts twice, making use of the bottom and top boundary conditions on $\psi(r,z)$. This procedure results in the radial structure problem

$$\frac{d}{dr}\left(\frac{d(r\psi_n)}{rdr}\right) - \mu_n^2\psi_n = \frac{g}{\theta_0 A}\frac{d\dot{\theta}_n}{dr}, \qquad \psi_n(0) = 0, \quad r\psi_n(r) \to 0 \text{ as } r \to \infty, \tag{3.4}$$

where μ_n, the inverse Rossby length, is defined by

$$\mu_n = \left(\frac{C}{A}\right)^{1/2}\frac{n\pi}{z_T} = \frac{n\pi}{\Gamma z_T}. \tag{3.5}$$

Because of (2.13), the right hand side of (3.4) vanishes for $r \neq r_1, r_2$, yielding the modified Bessel equation

$$r^2\frac{d^2\psi_n}{dr^2} + r\frac{d\psi_n}{dr} - \left(\mu_n^2 r^2 + 1\right)\psi_n = 0 \quad \text{for} \quad r \neq r_1, r_2. \tag{3.6}$$

The radial structure functions $\psi_n(r)$ must be continuous across $r = r_1$ and $r = r_2$, but the radial derivative of $\psi_n(r)$ is discontinuous, with the magnitude of the discontinuity determined by integration of (3.4) across very narrow radial intervals centered at $r = r_1$ and $r = r_2$. In this way we obtain the matching conditions

$$\left[\psi_n\right]_{r_1^-}^{r_1^+} = 0, \qquad \left[\frac{d(r\psi_n)}{rdr}\right]_{r_1^-}^{r_1^+} = \frac{g\dot{\Theta}_n}{\theta_0 A}, \qquad \left[\psi_n\right]_{r_2^-}^{r_2^+} = 0, \qquad \left[\frac{d(r\psi_n)}{rdr}\right]_{r_2^-}^{r_2^+} = -\frac{g\dot{\Theta}_n}{\theta_0 A}, \tag{3.7}$$

where the minus and plus superscripts denote points just to the left and right, and where $\dot{\Theta}_n$ is given by

$$\dot{\Theta}_n = \frac{2}{z_T}\int_0^{z_T}\dot{\Theta}(z)\sin\left(\frac{n\pi z}{z_T}\right)dz. \tag{3.8}$$

Using (2.14) in (3.8) and evaluating the resulting integral, we can obtain a computationally useful formula for $\dot{\Theta}_n$. The result is given below in (3.12).

Since it is a solution of (3.6) and (3.7), the nth radial structure function $\psi_n(r)$ can be written as the superposition of two radial structure functions, i.e., $\psi_n(r) = \psi_n^{(1)}(r) + \psi_n^{(2)}(r)$, where $\psi_n^{(1)}(r)$ satisfies the homogeneous equation (3.6) for $r \neq r_1$ and satisfies the matching conditions at $r = r_1$, and where $\psi_n^{(2)}(r)$ satisfies the homogeneous equation (3.6) for $r \neq r_2$ and satisfies the matching conditions at $r = r_2$. The function $\psi_n^{(1)}(r)$ is constructed from a combination of the order one modified Bessel functions $I_1(\mu_n r)$ and $K_1(\mu_n r)$. Because of the lateral boundary conditions given in (3.4), only the $I_1(\mu_n r)$ solution is valid for $0 \le r \le r_1$ and only the $K_1(\mu_n r)$ solution is valid for $r_1 \le r < \infty$. The jump conditions at $r = r_1$ can be enforced with the aid of the derivative relations $d[rI_1(\mu_n r)]/rdr = \mu_n I_0(\mu_n r)$ and $d[rK_1(\mu_n r)]/rdr = -\mu_n K_0(\mu_n r)$, and the Wronskian $I_0(\mu_n r)K_1(\mu_n r) + K_0(\mu_n r)I_1(\mu_n r) = 1/(\mu_n r)$. The result is given below in (3.10). The function $\psi_n^{(2)}(r)$ is constructed in a similar fashion, with the result given below in (3.11).

To summarize, for the case in which A and C are constants and $B = 0$, the solution of the transverse circulation problem (2.10) is

$$\psi(r,z) = \sum_{n=1}^{\infty}\left[\psi_n^{(1)}(r) + \psi_n^{(2)}(r)\right]\sin\left(\frac{n\pi z}{z_T}\right), \tag{3.9}$$

where

$$\psi_n^{(1)}(r) = -\frac{g\dot{\Theta}_n}{\theta_0}\frac{r_1}{A}\begin{cases} K_1(\mu_n r_1)I_1(\mu_n r) & \text{if} \quad 0 \le r \le r_1 \\ I_1(\mu_n r_1)K_1(\mu_n r) & \text{if} \quad r_1 \le r < \infty, \end{cases} \tag{3.10}$$

$$\psi_n^{(2)}(r) = \frac{g\dot{\Theta}_n}{\theta_0}\frac{r_2}{A}\begin{cases} K_1(\mu_n r_2)I_1(\mu_n r) & \text{if} \quad 0 \le r \le r_2 \\ I_1(\mu_n r_2)K_1(\mu_n r) & \text{if} \quad r_2 \le r < \infty, \end{cases} \tag{3.11}$$

$$\dot{\Theta}_n = \frac{2\dot{\Theta}_{\max}(z_2 - z_1)z_T}{\pi\left[z_T^2 - n^2(z_2 - z_1)^2\right]} \cdot\left[\sin\left(\frac{n\pi z_1}{z_T}\right) + \sin\left(\frac{n\pi z_2}{z_T}\right)\right], \tag{3.12}$$

with $\Gamma = (A/C)^{1/2}$ measuring the relative magnitudes of static stability and inertial stability. To compute $\psi(r,z)$ from (3.9)–(3.12) we must first specify the parameters $r_1, r_2, z_1, z_2, z_T, \dot{\Theta}_{\max}, A, C$. For the calculations presented here we have chosen $r_1 = 30$ km, $r_2 = 50$ km, $z_1 = 2$ km, $z_2 = 10$ km, $z_T = 5\pi$ km, $\dot{\Theta}_{\max} = 100$ K day^{-1}, $\rho_0 A = 1.64 \times 10^{-4}$ s^{-2} (see Fig. 1 of Schubert and Hack 1983), and the four values of C that result in $(A/C)^{1/2} = \Gamma = 256, 64, 16, 4$. The first case, $\Gamma = 256$, is typical of a resting atmosphere because, in that case, $(\rho_0 C)^{1/2} = (1/256)(\rho_0 A)^{1/2} \approx 5.0 \times 10^{-5}\text{s}^{-1} \approx f(20\text{N})$. The other three cases, $\Gamma = 64, 16, 4$, correspond to the progressively more intense vortices $(\rho_0 C)^{1/2} \approx 4f, 16f, 64f$.

Figure 3 shows isolines of $r\psi(r,z)$ for the four cases $\Gamma = 256, 64, 16, 4$. The spectrum of Rossby lengths μ_n^{-1} for $n = 1, 2, \ldots, 10$ is shown in Table 1 for these four cases. For the $\Gamma = 256$ case, the spectrum of Rossby lengths ranges from 1280 km for $n = 1$ to 128 km for $n = 10$. Since these Rossby lengths are all greater than r_1 and r_2, the secondary circulation is under strong control by the symmetry condition at $r = 0$. The result is that the inner cell is almost completely suppressed (i.e., very weak eye subsidence) while the lower tropospheric radial inflow and upper tropospheric radial outflow extend all the way to the inner edge of the eyewall. As we shall see in Section 4, the concept of Rossby depth is complementary to that of Rossby length, such that Rossby depths are small when Rossby lengths are large. In fact, for the $\Gamma = 256$ case, the Rossby depths are so small that the secondary circulation is under very weak control by the bottom and top boundary conditions.

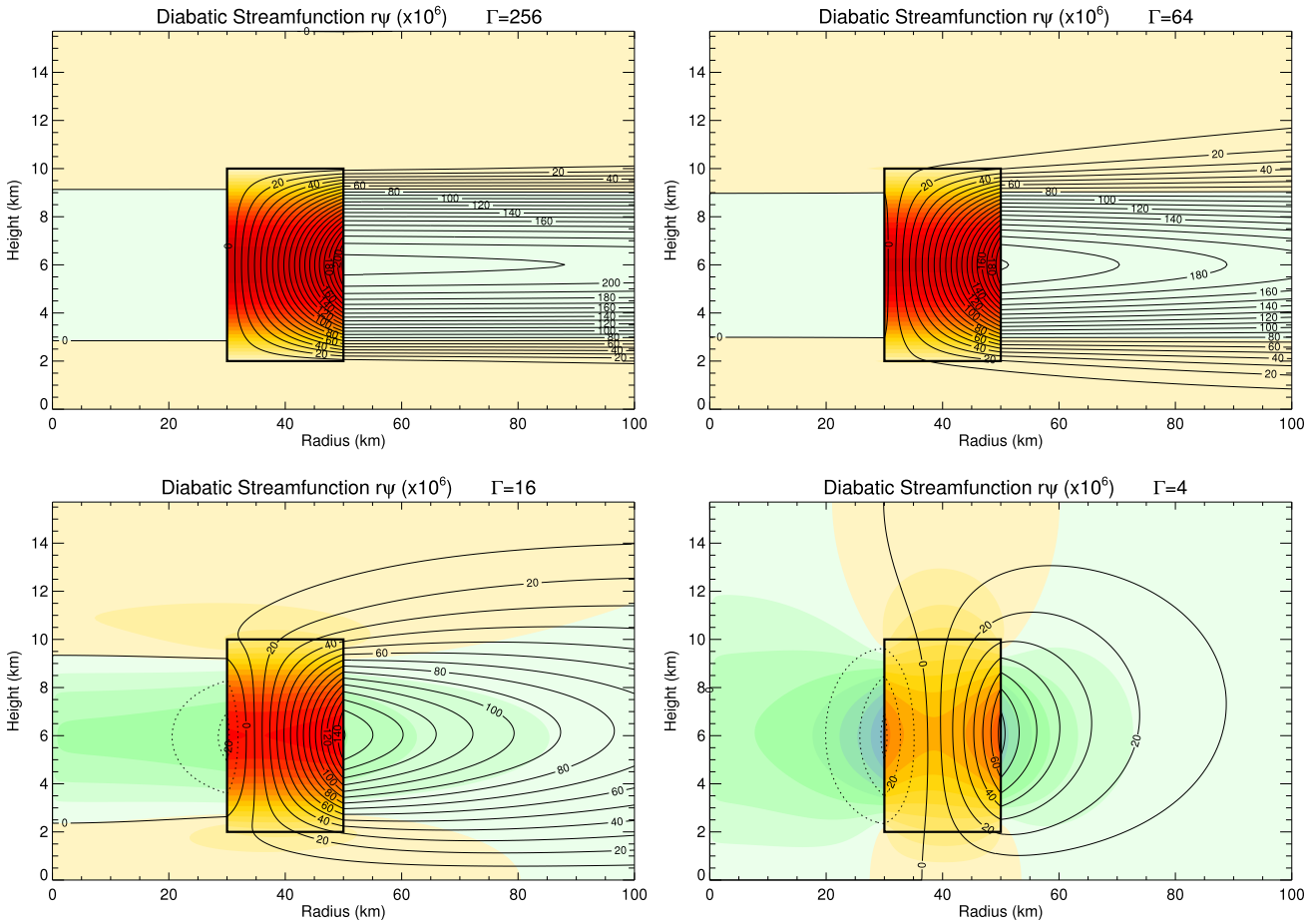

Figure 3. Line contours are isolines of $r\psi$ forced solely by diabatic heating. The sense of the circulation is counterclockwise for the dashed lines and clockwise for the solid lines. The four panels are created for $z_1 = 2$ km, $z_2 = 10$ km, $r_1 = 30$ km, $r_2 = 50$ km, $\dot{\Theta}_{\max} = 100$ K day^{-1}, and $\Gamma = 256, 64, 16, 4$. The black rectangle indicates the region of diabatic heating, as given by (2.13) and (2.14). Colored contours indicate ω, the vertical pressure velocity, which is related to w by $\omega = -g\rho w$, with ρ denoting the pseudodensity defined in Section 2. Warm colors are upward, cool colors are downward, and the contour interval is 5 hPa hr^{-1}.

As a tropical cyclone intensifies, the spectrum of Rossby lengths shifts to lower values while the spectrum of Rossby depths shifts to higher values. In the process, the transverse circulation becomes less controlled by the $r = 0$ boundary condition but increasingly controlled by the bottom and top boundary conditions. When $\Gamma = 4$ (lower right panel of Fig. 3), the total upward mass flux in the eyewall has been reduced to less than half of its value in the $\Gamma = 256$ case. Some of this reduction can be attributed to the increased influence of the bottom and top boundary conditions, but most of this reduction in upward mass flux is due to the strong inertial stiffening in the $\Gamma = 4$ case. This will be more clearly seen in Section 5, where the method of images separates the influence of the boundary conditions from the influence of the interior stiffening of the vortex.

The results of Fig. 3 suggest that eye formation can be viewed as a two-stage process. In the first stage, deep convection and the associated diabatic heating become confined to an annular ring, probably due to the fact that Ekman pumping maximizes away from the axis of the vortex, as discussed by Ooyama (1968, 1969), Eliassen (1971), Eliassen and Lystad (1977), Yamasaki (1977, his Fig. 9b), and Montgomery et al. (2001). However, even with diabatic heating confined to an annular ring, a vortex with $\Gamma = 64$ does not produce much subsidence inside $r = 30$ km (upper right panel of Fig. 3). Thus, the radar reflectivity pattern corresponding to the upper right panel would show an echo-free eye and an annular ring of strong echo, but an aircraft radial leg would not show an eye with large dewpoint depressions. As the vortex becomes stronger (bottom two panels of Fig. 3), almost the entire spectrum of Rossby lengths (right two columns of Table 1) shrink to less than 30 km. Subsidence then develops in the core, and, except for the very lowest troposphere, we would expect very large dewpoint depressions to develop in the core. In fact, if the vortex is strong enough, subsidence becomes concentrated near the outer edge of the eye, so we can expect the occurrence of the related phenomena of an eye moat, a hub cloud, and a warm ring thermal structure (Schu-

Table 1. The spectrum of Rossby lengths $\mu_n^{-1} = \Gamma z_T/(n\pi)$ for the four values of Γ listed in the top row and for the ten values of n listed in the left column. The Rossby lengths are given in kilometers (rounded to the nearest tenth of a kilometer) and have been computed using z_T =5π km. The case Γ =256 corresponds to a weak vortex, with Rossby lengths ranging from 128 km to 1280 km. The case Γ =4 corresponds to a strong vortex, with Rossby lengths ranging from 2 km to 20 km.

	Rossby Length (km)			
n	Γ = 256	Γ = 64	Γ = 16	Γ = 4
1	1280.0	320.0	80.0	20.0
2	640.0	160.0	40.0	10.0
3	426.7	106.7	26.7	6.7
4	320.0	80.0	20.0	5.0
5	256.0	64.0	16.0	4.0
6	213.3	53.3	13.3	3.3
7	182.9	45.7	11.4	2.9
8	160.0	40.0	10.0	2.5
9	142.2	35.6	8.9	2.2
10	128.0	32.0	8.0	2.0

bert et al. 2007). In addition, upper level radial inflow such as that shown in the lower right panel of Fig. 3 will tend to produce an upper level cloud overhang such as that observed in the CloudSat image shown in the bottom panel of Fig. 2. In summary, the first stage of eye formation involves the development of an annular ring of deep convection with little subsidence in the core, while the second stage involves the development of strong subsidence and desiccation in the core.

4. Arriving at ψ via the concept of Rossby depth

In Section 3 the $\psi(r,z)$ field was represented via (3.2) in terms of oscillatory functions of z, each of which had a coefficient $\psi_n(r)$ that was evanescent in r. In this section $\psi(r,z)$ is represented via (4.1) in terms of oscillatory functions of r, each of which has a coefficient $\hat{\psi}(k,z)$ that is evanescent in z, as given below in (4.6). These two approaches are complementary, each yielding its own type of physical insight. To solve (3.1) via the second approach, we introduce the Hankel transform pair

$$\psi(r,z) = \int_0^\infty \hat{\psi}(k,z) J_1(kr)\, k\, dk, \tag{4.1}$$

$$\hat{\psi}(k,z) = \int_0^\infty \psi(r,z) J_1(kr)\, r\, dr, \tag{4.2}$$

where $J_1(kr)$ is the order one Bessel function and k is the radial wavenumber. A similar transform pair exists for $\dot{\theta}(r,z)$ and $\hat{\dot{\theta}}(k,z)$. To take the Hankel transform of (3.1), we first multiply it by $rJ_1(kr)$ and integrate over all r. The integral originating from the first term in (3.1) is then integrated by parts twice, making use of the lateral boundary conditions on $\psi(r,z)$ and making use of the Bessel differential equation

$$\frac{d}{dr}\left(\frac{d[rJ_1(kr)]}{rdr}\right) = -k^2 J_1(kr). \tag{4.3}$$

This procedure results in the vertical structure problem

$$\begin{aligned} &\frac{d^2\hat{\psi}(k,z)}{dz^2} - \gamma^2(k)\hat{\psi}(k,z) \\ &\qquad = \frac{g}{\theta_0 C}\left[r_1 J_1(kr_1) - r_2 J_1(kr_2)\right]\dot{\Theta}(z), \\ &\hat{\psi}(k,0) = 0, \qquad \hat{\psi}(k,z_T) = 0, \end{aligned} \tag{4.4}$$

where $\gamma(k)$, the inverse of the Rossby depth, is defined by

$$\gamma(k) = \left(\frac{A}{C}\right)^{1/2} k = \Gamma k. \tag{4.5}$$

Note that (4.5) is the analogue of (3.5), with $\gamma^{-1}(k) = (C/A)^{1/2}k^{-1}$ giving the spectrum of Rossby depths as a function of the horizontal wavenumber k, and $\mu_n^{-1} = (A/C)^{1/2}(z_T/\pi)n^{-1}$ giving the spectrum of Rossby lengths as a function of the vertical wavenumber n.

Because $\dot{\Theta}(z)$ is given by (2.14), we must solve the homogeneous version of (4.4) in the two regions $0 \le z < z_1$ and $z_2 < z < z_T$, the inhomogeneous version of (4.4) in the region $z_1 < z < z_2$, and then match the solutions in such a way that $\hat{\psi}(k,z)$ and $d\hat{\psi}(k,z)/dz$ are continuous across $z = z_1$ and $z = z_2$. The result is

$$\hat{\psi}(k,z) = -\frac{g\pi\dot{\Theta}_{\max}\left[r_1 J_1(kr_1) - r_2 J_1(kr_2)\right]}{\theta_0 C\gamma(z_2-z_1)\left[\gamma^2 + \left(\frac{\pi}{z_2-z_1}\right)^2\right]2\left(1-e^{-2\gamma z_T}\right)}$$

$$\begin{cases} \left[\left(1-e^{-2\gamma z_1}\right)e^{-\gamma(z-z_1)} + \left(1-e^{-2\gamma z_2}\right)e^{-\gamma(z-z_2)}\right]\left(1-e^{-2\gamma(z_T-z)}\right) & \text{if} \quad z_2 \le z \le z_T, \\ \left(1-e^{-2\gamma z_1}\right)e^{-\gamma(z-z_1)}\left(1-e^{-2\gamma(z_T-z)}\right) + \left(1-e^{-2\gamma z}\right)e^{-\gamma(z_2-z)}\left(1-e^{-2\gamma(z_T-z_2)}\right) & \\ \qquad + 2\gamma\left(\frac{z_2-z_1}{\pi}\right)\left(1-e^{-2\gamma z_T}\right)\sin\left(\frac{\pi(z-z_1)}{z_2-z_1}\right) & \text{if} \quad z_1 \le z \le z_2, \\ \left[\left(1-e^{-2\gamma(z_T-z_1)}\right)e^{-\gamma(z_1-z)} + \left(1-e^{-2\gamma(z_T-z_2)}\right)e^{-\gamma(z_2-z)}\right]\left(1-e^{-2\gamma z}\right) & \text{if} \quad 0 \le z \le z_1. \end{cases} \tag{4.6}$$

Table 2. The spectrum of Rossby depths $\gamma^{-1}(k) = 1/(\Gamma k)$ for the four values of Γ listed in the top row and for the ten values of $1/k$ listed in the left column. The Rossby depths are given in kilometers, rounded to the nearest meter. The case Γ =256 corresponds to a weak vortex, with Rossby depths ranging from 31 m to 16 km. The case Γ =4 corresponds to a strong vortex, with Rossby depths ranging from 2 km to 1024 km.

	Rossby Depth (km)			
$1/k$ (km)	$\Gamma = 256$	$\Gamma = 64$	$\Gamma = 16$	$\Gamma = 4$
4096	16	64	256	1024
2048	8	32	128	512
1024	4	16	64	256
512	2	8	32	128
256	1	4	16	64
128	0.5	2	8	32
64	0.25	1	4	16
32	0.125	0.5	2	8
16	0.063	0.25	1	4
8	0.031	0.125	0.5	2

To summarize, for the case in which A and C are constants and $B = 0$, the solution of the transverse circulation problem (2.10) is (4.1), with $\hat{\psi}(k,z)$ given by (4.6). As a check on our solutions we have computed $\psi(r,z)$ from (4.1) and (4.6) and compared the results with $\psi(r,z)$ computed from (3.9)–(3.12). The results are identical since they are simply two different mathematical representations of the unique solution to (2.10). The solution method described in Section 3 begins with a vertical transform and then solves the radial structure equation (3.4), which contains the Rossby length μ_n^{-1} of each vertical wavenumber n. In contrast, the solution method described here in Section 4 begins with a horizontal transform and then solves the vertical structure equation (4.4), which contains the Rossby depth $\gamma^{-1}(k)$ of each horizontal wavenumber k. Since the Rossby length μ_n^{-1} is proportional to Γ and the Rossby depth $\gamma^{-1}(k)$ is proportional to $1/\Gamma$, these two concepts are complementary. Both are useful in understanding tropical cyclone development.

Table 2 gives the spectrum of Rossby depths for the four values of Γ used in Fig. 3. For the weak vortex case ($\Gamma = 256$), the spectrum of Rossby depths ranges from 1000 m for k^{-1} = 256 km to 31 m for k^{-1} = 8 km, which explains why the secondary circulation does not extend above or below the heat source in the upper left panel of Fig. 3. In the strong vortex case ($\Gamma = 4$) the spectrum of Rossby depths shifts to larger values, so the secondary circulation extends above and below the heat source, although its extent below the source is limited by the lower boundary condition. In the top two panels of Fig. 3 the Rossby depths tend to be smaller than z_1 and $z_T - z_2$, so the secondary circulation is only weakly controlled by the bottom and top boundary conditions.

We note in passing that the transform methods used in this section and the previous section depend on the assumption of constant coefficients in the transverse circulation equation. This assumption is probably acceptable for A, but is less justifiable for C. As a hurricane intensifies, the inertial stability coefficient C becomes very large in the hurricane core, but remains relatively unchanged in the far-field. Thus, the strong vortex case shown in the bottom right panel of Fig. 3 has unrealistically large C at the outer radii. With a more realistic, radially varying C, the outer part of the cross-section in the lower right panel would look more like the outer part of the lower left panel. Thus, the idealized analytic solutions presented here provide only an approximate quantitative guide to the complementary concepts of the spectrum of Rossby lengths and the spectrum of Rossby depths. In particular, the solutions help us understand the dynamical consequences of the enormous variability of C in hurricanes.

5. Arriving at ψ via a Green's function method

A third route (see Eliassen 1952, 1959, Shapiro and Willoughby 1982) to understanding the solutions of the elliptic problem (2.10) is through direct solution of the second order equation, ignoring the boundary conditions at $r = 0$ and $z = 0, z_T$. We again assume that A and C are constants, but now allow for nonzero B. Later in this section we shall enforce the lower boundary condition through the addition of an "image circulation" centered below the earth's surface. One advantage of this approach is that we obtain a better understanding of the role of B. A second advantage is that we obtain solutions with and without boundary conditions, so the role of the boundary conditions is clarified. We begin by noting that, when r is large enough that curvature effects are negligible, (2.10) reduces to

$$A\frac{\partial^2\psi}{\partial x^2} + 2B\frac{\partial^2\psi}{\partial x\partial z} + C\frac{\partial^2\psi}{\partial z^2} = \frac{g}{\theta_0}\frac{\partial\dot{\theta}}{\partial x}, \tag{5.1}$$

where $x = r - r_0$ is a cartesian coordinate with origin at $r = r_0$. We now transform to the skew coordinates $(\hat{x},\hat{z})$, which are defined by $\hat{x} = (Cx - Bz)/D$ and $\hat{z} = z$, where $D = (AC - B^2)^{1/2}$. Using $(\partial/\partial x) = (C/D)(\partial/\partial\hat{x})$ and $(\partial/\partial z) = (\partial/\partial\hat{z}) - (B/D)(\partial/\partial\hat{x})$, (5.1) then transforms to

$$\frac{\partial^2\psi}{\partial\hat{x}^2} + \frac{\partial^2\psi}{\partial\hat{z}^2} = \frac{g}{\theta_0 D}\frac{\partial\dot{\theta}}{\partial\hat{x}}. \tag{5.2}$$

Consider a diabatic heating field given by

$$\dot{\theta}(\hat{x},\hat{z}) = \begin{cases} \dot{\theta}_0 & \text{if } (\hat{z}-\hat{z}_0)^2/a^2 + \hat{x}^2/b^2 \le 1, \\ 0 & \text{if } (\hat{z}-\hat{z}_0)^2/a^2 + \hat{x}^2/b^2 > 1, \end{cases} \tag{5.3}$$

where the constant $\dot{\theta}_0$ specifies the uniform diabatic heating within the elliptical patch whose center is at $(\hat{x},\hat{z}) = (0,\hat{z}_0)$ and whose shape is specified by the constants a, b. Note that, with diabatic heating of the form (5.3), the right hand side of (5.2) vanishes everywhere except along the boundary of the elliptical patch.

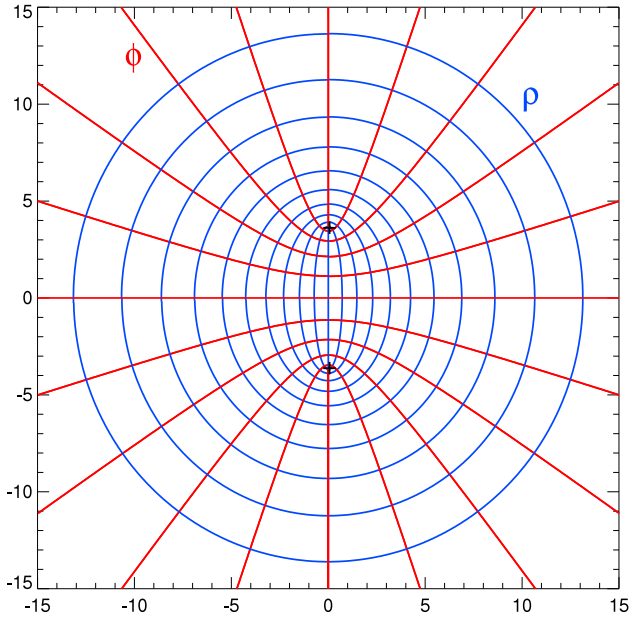

Figure 4. Elliptic coordinates (ρ, φ), as defined in (5.4). Lines of constant ρ (blue) are the ellipses and lines of constant φ (red) are the hyperbolas. Both sets of curves have the same foci, located at $(\hat{x}, \hat{z} - \hat{z}_0) = (0, \pm c)$ and indicated by the + symbols. Far from the origin, lines of constant ρ are very nearly circles and lines of constant φ are very nearly straight radials. The units on the axes are in km, and only select values of ρ and φ are shown for clarity.

To derive the solution of (5.2), it is convenient to use the elliptic coordinates (ρ, φ), which are related to the skew coordinates by $(\hat{z} - \hat{z}_0) + i\hat{x} = c\,\cosh(\rho + i\varphi)$, or equivalently,

$$\hat{x} = c\,\sinh\rho\,\sin\varphi, \quad \hat{z} - \hat{z}_0 = c\,\cosh\rho\,\cos\varphi, \tag{5.4}$$

where $c = (a^2 - b^2)^{1/2}$. From (5.4) it is easily shown that

$$\frac{\hat{x}^2}{c^2\sinh^2\rho} + \frac{(\hat{z} - \hat{z}_0)^2}{c^2\cosh^2\rho} = 1, \tag{5.5}$$

and

$$\frac{(\hat{z} - \hat{z}_0)^2}{c^2\cos^2\varphi} - \frac{\hat{x}^2}{c^2\sin^2\varphi} = 1, \tag{5.6}$$

so that the lines of constant ρ are ellipses and the lines of constant φ are hyperbolas (see Fig. 4). The complete family of ellipses is generated by allowing the coordinate ρ to vary over the range $0 \le \rho < \infty$, while the complete family of hyperbolas is generated by allowing the coordinate φ to vary over the range $0 \le \varphi \le 2\pi$. In particular, the ellipse $(\hat{z} - \hat{z}_0)^2/a^2 + \hat{x}^2/b^2 = 1$, which just encloses the region of nonzero diabatic heating, is specified by $\rho = \rho_0 = \tanh^{-1}(b/a) = \frac{1}{2}\ln[(a+b)/(a-b)]$. As ρ becomes very large, $\cosh\rho \approx \sinh\rho \approx \frac{1}{2}e^{\rho}$, so that the lines of constant ρ approach circles with radius $\frac{1}{2}ce^{\rho}$ in the skew-coordinate space, and the lines of constant φ approach the straight radials $\varphi = \tan^{-1}[\hat{x}/(\hat{z} - \hat{z}_0)]$.

Expressed in terms of the elliptic coordinates, the diabatic heating (5.3) is

$$\dot{\theta}(\rho) = \begin{cases} \dot{\theta}_0 & \text{if } \rho \le \rho_0, \\ 0 & \text{if } \rho > \rho_0, \end{cases} \tag{5.7}$$

and the governing equation (5.2) is

$$\frac{\partial^2\psi}{\partial\rho^2} + \frac{\partial^2\psi}{\partial\varphi^2} = \frac{gc}{\theta_0 D}\cosh\rho\,\sin\varphi\,\frac{\partial\dot{\theta}}{\partial\rho}, \tag{5.8}$$

where we have used $(\partial\dot{\theta}/\partial\varphi) = 0$, which follows from (5.7). The right hand side of (5.8) vanishes for $\rho \ne \rho_0$, so that to obtain the streamfunction corresponding to the diabatic heating (5.3) we must solve

$$\frac{\partial^2\psi}{\partial\rho^2} + \frac{\partial^2\psi}{\partial\varphi^2} = 0 \quad \text{for} \quad \rho \ne \rho_0, \tag{5.9}$$

then enforce the far-field boundary condition, and finally match the solutions at $\rho = \rho_0$ in such a way that ψ is continuous, but $(\partial\psi/\partial\rho)$ has a discontinuity whose magnitude is determined by integrating (5.8) over a very narrow interval of ρ centered at $\rho = \rho_0$. Thus, the matching conditions are

$$[\psi]_{\rho_0^-}^{\rho_0^+} = 0 \quad \left[\frac{\partial\psi}{\partial\rho}\right]_{\rho_0^-}^{\rho_0^+} = -\frac{gc\dot{\theta}_0}{\theta_0 D}\cosh\rho_0\,\sin\varphi, \tag{5.10}$$

where the minus and plus superscripts denote points just inside and just outside ρ_0.

As is easily confirmed by direct substitution, the solution of (5.9) and (5.10) is

$$\psi(\rho,\varphi) = \frac{gc\dot{\theta}_0}{\theta_0 D}\cosh\rho_0\,\sin\varphi\begin{cases} e^{-\rho_0}\sinh\rho & \text{if } \rho \le \rho_0, \\ e^{-\rho}\sinh\rho_0 & \text{if } \rho \ge \rho_0. \end{cases} \tag{5.11}$$

Since the term in the second line of (5.11) decays exponentially with ρ, the far-field boundary condition is satisfied. The $\psi(\rho,\varphi)$ field given by (5.11) is continuous at $\rho = \rho_0$. Similarly, we can show that $\partial\psi/\partial\rho$ satisfies the jump condition given in (5.10). Thus, (5.11) is the solution of (5.9) satisfying the desired boundary and interface conditions.

Plots of $\psi(x,z)$ can be obtained by choosing a regular grid of (x,z) points, then finding the corresponding values of $\rho(x,z), \varphi(x,z)$ from

$$\rho(x,z) + i\varphi(x,z) = \cosh^{-1}\left(\frac{D(z - z_0) + i(Cx - Bz)}{D(a^2 - b^2)^{1/2}}\right), \tag{5.12}$$

and finally using (5.11) to compute $\psi(\rho(x,z), \varphi(x,z))$. Isolines of ψ, as determined from (5.11) and (5.12), are plotted in Fig. 5 for the case $a = 4$ km, $b = (C/D)10$ km, $\hat{z}_0 = 6$ km, $\dot{\theta}_0 = 100$ K day^{-1}, and $\Gamma = 4$. The top panel is for a barotropic vortex ($B = 0$), so the updraft does not tilt with height. The bottom panel is for a baroclinic vortex with $-B/C = 1$, so that, according to (2.12), the angular momentum surfaces have a tilt of 45°. Within the heated region, the isolines of ψ tend to follow the angular momentum surfaces, so the updraft tilt is approximately 45°, the same as that for the inner eyewall of

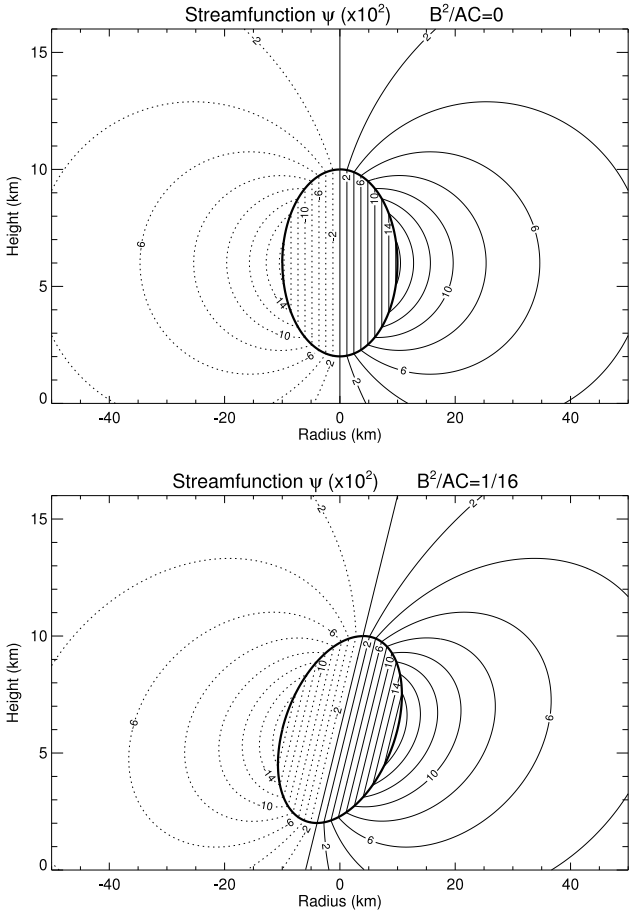

Figure 5. Isolines of ψ, as determined from (5.11), for the case $a = 4$ km, $b = (C/D)10$ km, $\hat{z}_0 = 6$ km, $\dot{\theta}_0 = 100$ K day^{-1}, and $\Gamma = 4$. The top panel is for a barotropic vortex ($B = 0$), while the bottom panel is for a baroclinic vortex with $-B/C = 1$, in which case an angular momentum surface in the eyewall has a slope of 45°.

Typhoon Choi-Wan, as shown in Fig. 2. According to (5.11), the strength of the overturning circulation is inversely proportional to D. Since the value of D is approximately 3% smaller in the lower panel of Fig. 5, the overturning circulation in the baroclinic vortex is only slightly stronger than that in the barotropic vortex. This result is typical for tropical cyclone situations and leads to the conclusion that the vortex baroclinity is crucial for updraft tilt but has only a small effect on updraft strength.

The ψ fields displayed in Fig. 5, having been computed using (5.11), do not satisfy the lower boundary condition $\psi = 0$. A solution of (5.8) that does satisfy the lower boundary condition can be constructed by superposition of (5.11) and its image, which is the ψ field associated with a negative heat source centered below the earth's surface at $(\hat{x}, \hat{z}) = (0, -\hat{z}_0)$. This image solution is easily computed from a modified version of (5.11), obtained by changing $\dot{\theta}_0$ to $-\dot{\theta}_0$ and $\hat{z}_0$ to $-\hat{z}_0$. For $\Gamma = 4$ and $B^2/(AC) = 1/16$, this image solution is shown by the red lines in the top panel of Fig. 6, with the original solution shown by the blue lines. The superposition of these two patterns, neither of which satisfies the boundary condition, results in the solution shown in the bottom panel, which does satisfy both the governing equation (5.8) and the $\psi = 0$ boundary condition. An important feature of Fig. 6 is that the red image solution does not penetrate very far into the interior, which means that the enforcement of the lower boundary condition only modifies the solution in the lowest few kilometers, causing the ψ contours to accommodate to the $\psi = 0$ condition at $z = 0$.

We are now in a position to answer the following question. Why is the total upward mass flux so much smaller in the lower right panel of Fig. 3 (a strong vortex with $\Gamma = 4$) than in the upper left panel (a weak vortex with $\Gamma = 256$). Is it due to (i) the large increase of inertial stability in the interior for the $\Gamma = 4$ case, or (ii) the larger influence of the upper and lower boundary conditions when Rossby depths become large in the $\Gamma = 4$ case? The answer appears to be (i), with the

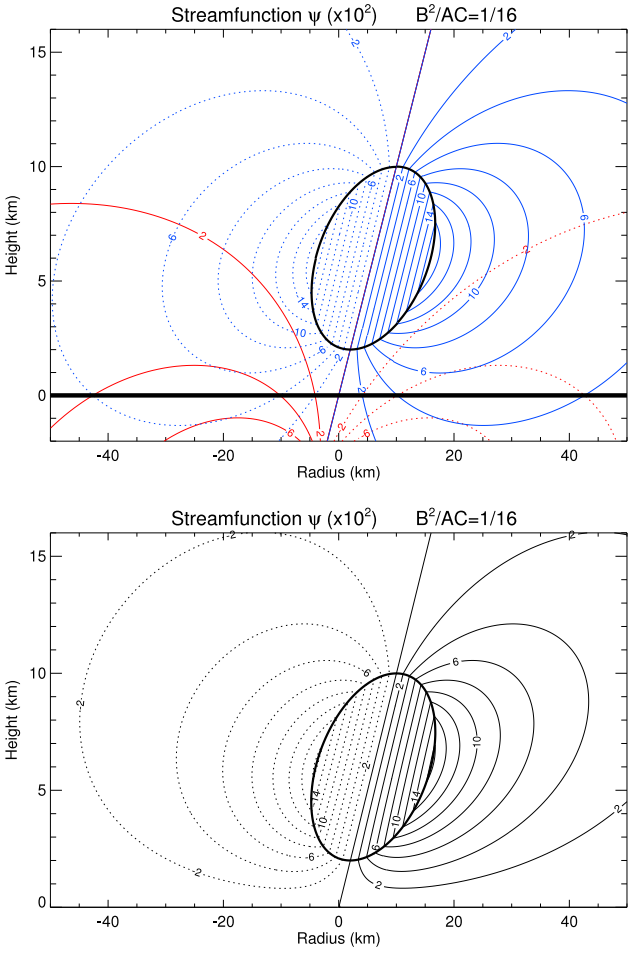

Figure 6. The isolines of ψ, as determined from (5.11), for the case $a = 4$ km, $b = (C/D)10$ km, $\dot{\theta}_0 = 100$ K day^{-1}, $\Gamma = 4$, and $B^2/(AC) = 1/16$. In the top panel, the elliptical region of heating is shown in black, its associated streamfunction is shown in blue, and the corresponding ficticious 'image' circulation is shown in red. The bottom panel shows the sum of the two circulations, which satisfies the lower boundary condition.

boundary conditions exerting only weak control on the total upward mass flux. This becomes obvious by noting that the strength of the transverse circulation in the bottom panel of Fig. 6 (lower boundary condition enforced) is nearly the same as that in the bottom panel of Fig. 5 (lower boundary condition not enforced).

6. Upward penetration of Ekman pumping

So far we have neglected the effects of friction on the transverse circulation. Although the direct effects of friction are confined primarily to the lowest kilometer, the "inviscid interior" is indirectly affected by boundary layer friction through the secondary circulation resulting from the Ekman pumping at the top of the boundary layer. As discussed in this section, the spatial structure of the frictionally driven interior circulation depends on the vortex strength and can be understood using the concept of a spectrum of Rossby depths. To understand how the upward penetration of Ekman pumping depends on vortex strength, consider a modified version of the problem (2.10). Again assume that $B = 0$ and that A and C are constants, but now assume that $\dot{\theta} = 0$ and that a nonzero streamfunction is specified at the lower boundary $z = z_B$, the top of the Ekman layer. Assume the Ekman pumping at the top of the boundary layer is given by

$$w(r, z_B) = w_0 \alpha r \left(1 - \tfrac{1}{3}\alpha r\right) e^{-\alpha r}, \tag{6.1}$$

where the constant w_0 is proportional to the magnitude of the vertical velocity, and the constant α is related to the size of the region of pumping. This structure places zero vertical motion at $r = 0$, an upward maximum at $r = (5 - \sqrt{13})/(2\alpha)$, zero at $r = 3/\alpha$, maximum downward motion at $r = (5 + \sqrt{13})/(2\alpha)$, and $w \to 0$ as $r \to \infty$. The resulting elliptic problem for the transverse circulation is

$$\begin{aligned} &A\frac{\partial}{\partial r}\left(\frac{\partial(r\psi)}{r\partial r}\right) + C\frac{\partial^2\psi}{\partial z^2} = 0, \\ &\psi(0, z) = 0, \qquad \psi(r, z_T) = 0, \\ &\psi(r, z_B) = \tfrac{1}{3}\rho_B w_0 \alpha r^2 e^{-\alpha r}, \\ &r\psi(r, z) \to 0 \quad \text{as} \quad r \to \infty, \end{aligned} \tag{6.2}$$

where $\psi(r, z_B)$ has been obtained by integration of (6.1). To solve (6.2) we follow the Hankel transform procedure of Section 4. This procedure results in the vertical structure problem

$$\begin{aligned} &\frac{d^2\hat{\psi}(k, z)}{dz^2} - \gamma^2(k)\hat{\psi}(k, z) = 0, \\ &\hat{\psi}(k, z_T) = 0, \quad \hat{\psi}(k, z_B) = \rho_B w_0 \frac{\alpha k(4\alpha^2 - k^2)}{(\alpha^2 + k^2)^{7/2}}, \end{aligned} \tag{6.3}$$

where $\gamma(k)$ is given in (4.5), and where $\hat{\psi}(k, z_B)$ has been obtained by substituting the expression for $\psi(r, z_B)$ into (4.2) and evaluating the resulting integral using Gradshteyn and Ryzhik (1994, page 733). The solution of (6.3) is

$$\hat{\psi}(k, z) = \left(\frac{e^{-\gamma(z - z_B)} - e^{-\gamma(2z_T - z - z_B)}}{1 - e^{-2\gamma(z_T - z_B)}}\right)\hat{\psi}(k, z_B). \tag{6.4}$$

The final solution for $\psi(r, z)$ is obtained by substituting (6.4) into (4.1) and numerically evaluating the resulting integral over k. The final solution for the vertical mass flux $\rho w(r, z)$ can be obtained in a similar fashion from

$$\rho w(r, z) = \int_0^\infty \hat{\psi}(k, z) J_0(kr)\, k^2\, dk, \tag{6.5}$$

which follows from (2.9), (4.1), and the Bessel function derivative relation

$$\frac{d[rJ_1(kr)]}{rdr} = kJ_0(kr). \tag{6.6}$$

Figure 7 shows isolines of $r\psi(r, z)$ for $z_B = 1$ km, $z_T = 5\pi$ km, $\alpha = 0.0465$ km^{-1}, and for the four cases $\Gamma = 256, 64, 16, 4$. Also shown in Fig. 7 are colored contours, which indicate the vertical pressure velocity $\omega = -g\rho w$. For comparison purposes concerning the depth of the penetration, we have used the same normalization factor $w_0 = 3.75$ m s^{-1} in all four panels, although of course the strength of the pumping should depend on the vortex strength. With $\alpha = 0.0465$ km^{-1}, upward Ekman pumping occurs in the region inside $r = 3/\alpha \approx 65$ km, with the maximum at $r \approx 15$ km. For the weak vortex case ($\Gamma = 256$) the corresponding values of the Rossby depths (second column of Table 2) are so small that the frictionally pumped fluid returns outward in a thin layer below 2 km. In contrast, for the strong vortex case ($\Gamma = 4$) the corresponding values of the Rossby depths (last column of Table 2) are so large that the frictionally pumped fluid penetrates to the tropopause. The smaller Rossby depths associated with smaller horizontal scales result in a marked smoothing effect as one moves upward, i.e., only the smooth horizontal components of the Ekman pumping reach the upper troposphere. A consequence of this smoothing effect is apparent in the color contours of the upward mass flux, which show a maximum at $r \approx 15$ km for $z = 1$ km, but switches to a maximum at $r = 0$ at higher levels, with the rapidity of the changeover depending on the value of Γ. This effect tends to reduce the ability of Ekman pumping at $z = 1$ km to determine the eyewall radius.

These results have implications for classic parameterization schemes (e.g., Ooyama 1969) that relate the activity of deep convection to the vertical velocity at the top of the boundary layer. Such schemes do not distinguish between physical situations with quite different Rossby depths. In fact, such classic parameterization schemes would seem more plausible for strong vortex situations where there is deep vertical penetration of Ekman pumping.

7. Concluding remarks

We have presented three different approaches to the solution of the transverse circulation equation (2.10), in the special case when the coefficients A, B, C are constants. All three approaches can contribute to our physical understanding of key

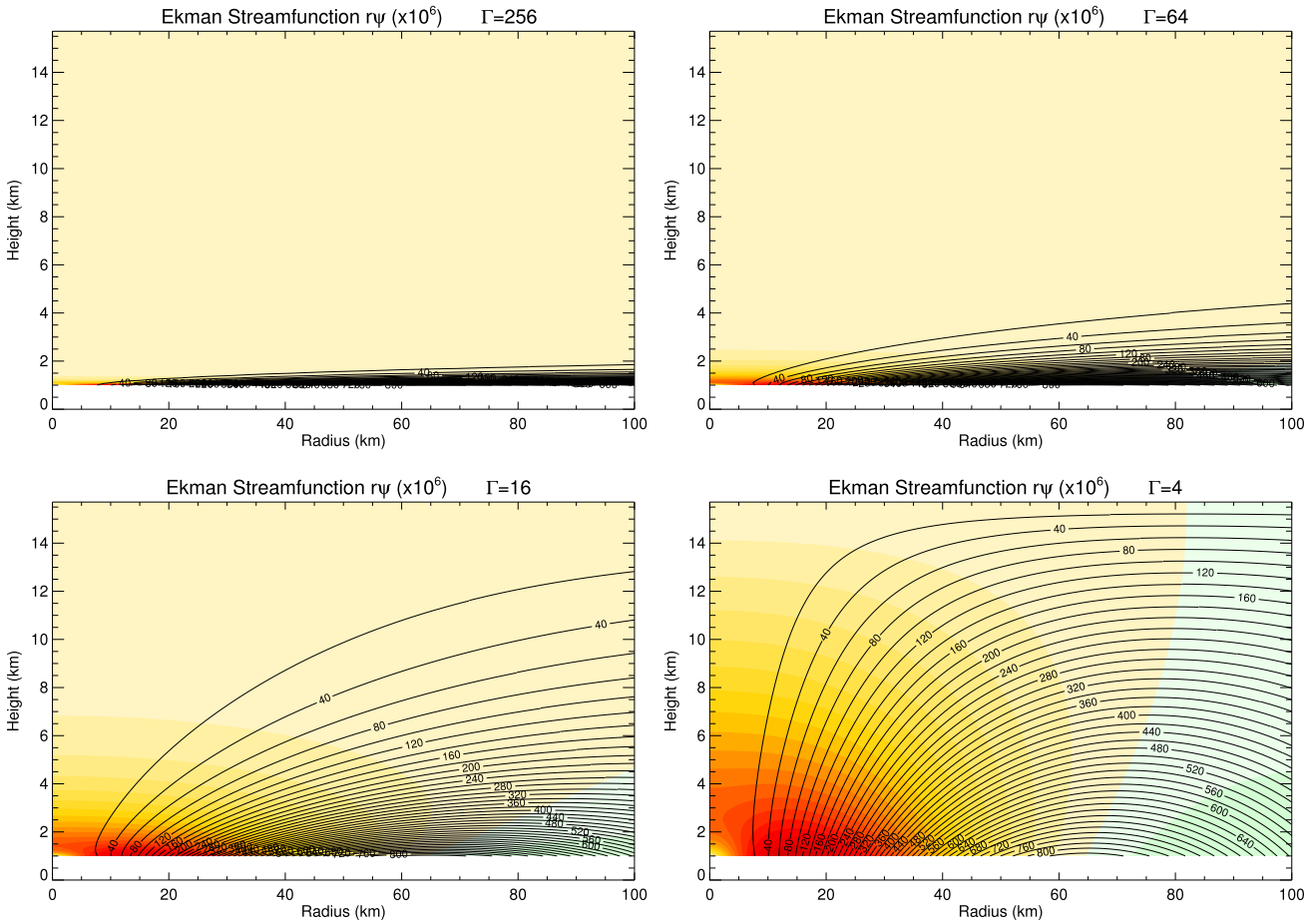

Figure 7. Line contours are isolines of $r\psi$ forced solely by Ekman pumping. The sense of the circulation is clockwise. The four panels are created for $z_B = 1$ km, $z_T = 5\pi$ km, $\alpha = 0.0465$ km^{-1}, $w_0 = 3.75$ m s^{-1}, and $\Gamma = 256, 64, 16, 4$. Colored contours indicate the vertical pressure velocity ω, which is related to the log-pressure vertical velocity w and the pseudodensity ρ by $\omega = -g\rho w$. Warm colors are upward, cool colors are downward, and the contour interval is 20 hPa hr^{-1}.

concepts such as Rossby length, Rossby depth, baroclinic eyewall tilt, the role of boundary conditions, upward penetration of Ekman pumping, and dynamical eye size. For example, the last of these concepts aids in understanding why the strength of the subsidence field in the eye can vary considerably as a vortex intensifies (Fig. 3), even if the diabatic heating remains nearly fixed. To see this, note that, in the $(A/C)^{1/2} = 64$ case, the first ten Rossby lengths (third column of Table 1) are all greater than the eye radius, while in the $\Gamma = (A/C)^{1/2} = 4$ case, the first ten Rossby lengths (last column of Table 1) are all less than the eye radius. In both cases the eye radius is 30 km, but in the case $\Gamma = (A/C)^{1/2} = 64$ this 30 km radius can be considered dynamically small (measured in Rossby lengths), while in the $(A/C)^{1/2} = 4$ case, this same 30 km eye radius can be considered dynamically large. Dynamically small eyes cannot accomodate intense subsidence because the symmetry condition at $r = 0$ is "too close", i.e., there is "not enough room" in the eye. In contrast, dynamically large eyes can accomodate intense subsidence, with expected large dewpoint depressions. Storms with dynamically large eyes can also produce eye moats, hub clouds, a warm ring thermal structure, and an upper level cloud overhang at the outer edge of the eye (in the bottom panel of Fig. 2, notice the inward-penetrating cloud overhang at 14 km altitude).

The results presented here also have implications for understanding the role of vortex preconditioning before the occurrence of rapid development. The importance of preconditioning is apparent in the work of Nolan (2007), who studied the development of a tropical cyclone from a weak vortex using high-resolution, cloud-resolving, nonhydrostatic numerical simulations. He found that, after the inner core has become humidified and a mid-level 7 m s^{-1} vortex has developed, a smaller scale vortex forms rapidly near the surface. This smaller vortex becomes the core of the intensifying tropical cyclone. The important role of a weak transverse circulation in the rapid development of a small-scale low-level vortex can be seen as follows. Consider a fluid particle that moves radially inward from radius r_1 to radius r_2, conserving absolute angular momentum so that $r_2 v_2 + \frac{1}{2} f r_2^2 = r_1 v_1 + \frac{1}{2} f r_1^2$, where we assume $f = 5 \times 10^{-5}$ s^{-1}. If $r_2 = 10$ km and $v_2 = 20$ m

s^{-1}, then r_1 = 90 km if the particle is initially at rest (v_1 = 0). However, for the same r_2 and v_2, we find that r_1 = 26.4 km if the azimuthal velocity has the "preconditioned" value v_1 = 7 m s^{-1}. For a radial inflow of 0.25 m s^{-1}, the first case requires approximately 89 hr for its 80 km inward shift, while the preconditioned case requires only 18 hr for its 16.4 km inward shift. Thus, a vortex with 7 m s^{-1} lower tropospheric azimuthal winds in its inner region is preconditioned for rapid development if diabatic processes can force a weak (~ 0.25 m s^{-1}) radial inflow in the inner region just above the frictional boundary layer. This example reemphasizes the importance of understanding the underlying dynamical principles associated with the derivation and solution of the transverse circulation equation (2.10).

Acknowledgments: We would like to thank Rick Taft for his assistance and two anonymous reviewers for their feedback that improved the paper. This research has been supported by the Office of Naval Research under contract N00014-10-1-0145, and by the National Science Foundation through grant ATM-0837932 and through the Center for Multi-Scale Modeling of Atmospheric Processes, managed by Colorado State University through cooperative agreement No. ATM-0425247. The calculations were made on workstations provided through a gift from the Hewlett-Packard Corporation.

References

Eliassen, A., 1952: Slow thermally or frictionally controlled meridional circulations in a circular vortex. *Astrophysica Norvegica*, **5**, 19–60.

Eliassen, A., 1959: On the formation of fronts in the atmosphere. *The Atmosphere and the Sea in Motion; Scientific Contributions to the Rossby Memorial Volume.* Edited by B. Bolin, Rockefeller Institute Press, New York, pages 277–287.

Eliassen, A., 1971: On the Ekman layer in a circular vortex. *J. Meteor. Soc. Japan*, **49**, 784–789.

Eliassen, A., and M. Lystad, 1977: The Ekman layer of a circular vortex: A numerical and theoretical study. *Geophys. Norv.*, **31**, 1–16.

Gradshteyn, I. S., and I. M. Ryzhik, 1994: Table of Integrals, Series, and Products. Fifth Edition. Academic Press, 1204 pages.

Hack, J. J., and W. H. Schubert, 1986: Nonlinear response of atmospheric vortices to heating by organized cumulus convection. *J. Atmos. Sci.*, **43**, 1559–1573, doi:10.1175/1520-0469(1986)043<1559:NROAVT>2.0.CO;2.

Montgomery, M. T., H. D. Snell, and Z. Yang, 2001: Axisymmetric spindown dynamics of hurricane-like vortices. *J. Atmos. Sci.*, **58**, 421–435, doi:10.1175/1520-0469(2001)058<0421:ASDOHL>2.0.CO;2.

Nolan, D. S., 2007: What is the trigger for tropical cyclogenesis? *Aust. Met. Mag.*, **56**, 241–266.

Nolan, D. S., Y. Moon, and D. P. Stern 2007: Tropical cyclone intensification from asymmetric convection: Energetics and efficiency. *J. Atmos. Sci.*, **64**, 3377–3405, doi:10.1175/JAS3988.1.

Ooyama, K., 1968: Numerical simulation of tropical cyclones with an axisymmetric model. *Proceedings of the WMO/IUGG Symposium on NWP*, Tokyo, 81–88.

Ooyama, K., 1969: Numerical simulation of the life cycle of tropical cyclones. *J. Atmos. Sci.*, **26**, 3–40, doi:10.1175/1520-0469(1969)026<0003:NSOTLC>2.0.CO;2.

Pendergrass, A. G., and H. E. Willoughby, 2009: Diabatically induced secondary flows in tropical cyclones. Part I: Quasi-steady forcing. *Mon. Wea. Rev.*, **137**, 805–821, doi:10.1175/2008MWR2657.1.

Schubert, W. H., and J. J. Hack, 1982: Inertial stability and tropical cyclone development. *J. Atmos. Sci.*, **39**, 1687–1697, doi:10.1175/1520-0469(1982)039<1687:ISATCD>2.0.CO;2.

Schubert, W. H., and J. J. Hack, 1983: Transformed Eliassen balanced vortex model. *J. Atmos. Sci.*, **40**, 1571–1583, doi:10.1175/1520-0469(1983)040<1571:TEBVM>2.0.CO;2.

Schubert, W. H., C. M. Rozoff, J. L. Vigh, B. D. McNoldy, and J. P. Kossin, 2007: On the distribution of subsidence in the hurricane eye. *Quart. J. Roy. Meteor. Soc.*, **133**, 595–605, doi:10.1002/qj.49.

Shapiro, L. J., and H. E. Willoughby, 1982: The response of balanced hurricanes to local sources of heat and momentum. *J. Atmos. Sci.*, **39**, 378–394, doi:10.1175/1520-0469(1982)039<0378:TROBHT>2.0.CO;2.

Smith, R. K., 1981: The cyclostrophic adjustment of vortices with application to tropical cyclone modification. *J. Atmos. Sci.*, **38**, 2021–2030, doi:10.1175/1520-0469(1981)038<2021:TCAOVW>2.0.CO;2.

Sundqvist, H., 1970a: Numerical simulation of the development of tropical cyclones with a ten-level model. Part I, *Tellus*, **22**, 359–390, doi:10.1111/j.2153-3490.1970.tb00503.x.

Sundqvist, H., 1970b: Numerical simulation of the development of tropical cyclones with a ten-level model. Part II. *Tellus*, **22**, 504–510, doi:10.1111/j.2153-3490.1970.tb00516.x.

Vigh, J. L., and W. H. Schubert, 2009: Rapid development of the tropical cyclone warm core. *J. Atmos. Sci.*, **66**, 3335–3350, doi:10.1175/2009JAS3092.1.

Willoughby, H. E., 2009: Diabatically induced secondary flows in tropical cyclones. Part II: Periodic forcing. *Mon. Wea. Rev.*, **137**, 822–835, doi:10.1175/2008MWR2658.1.

Yamasaki, M., 1977: The role of surface friction in tropical cyclones. *J. Meteor. Soc. Japan*, **55**, 559–571.